Mn local structure effects in charge-ordered mixed-valence $RE_{1-x}Ca_xMnO_3$ (RE: La, Tb) perovskites: a review of the experimental situation

2002 J. Phys.: Condens. Matter 14 5017

(http://iopscience.iop.org/0953-8984/14/19/323)

INSTITUTE OF PHYSICS PUBLISHING JOURNAL OF PHYSICS: CONDENSED MATTER

J. Phys.: Condens. Matter **14** (2002) 5017–5033 PII: S0953-8984(02)28949-3

Mn local structure effects in charge-ordered mixed-valence $RE_{1-x}Ca_xMnO_3$ (RE: La, Tb) perovskites: a review of the experimental situation

Gloria Subías[1,2,3], Joaquín García[2], Javier Blasco[2], M Concepción Sánchez[2] and M Grazia Proietti[2]

[1] European Synchrotron Radiation Facility, BP-220, F-38043 Grenoble, France
[2] Instituto de Ciencia de Materiales de Aragón, CSIC–Universidad de Zaragoza, C/Pedro Cerbuna 12, 50009-Zaragoza, Spain

E-mail: gsubias@esrf.fr

Received 19 September 2001, in final form 25 March 2002
Published 2 May 2002
Online at stacks.iop.org/JPhysCM/14/5017

Abstract

An extensive extended x-ray absorption fine-structure (EXAFS) study at the Mn K edge of the $La_{1-x}Ca_xMnO_3$ and $Tb_{1-x}Ca_xMnO_3$ ($x \geqslant 0.5$) series, as a function of temperature up to values around 600 K, has been performed. An accurate multiple-scattering analysis has been carried out; it shows that the paramagnetic phase ($T > 300$ K) of the so-called charge-ordered manganites is characterized by a random distribution of distorted octahedra, the distortion being less than the Jahn–Teller distortion of the undoped compounds. No significant changes are found for the first coordination shell (Mn–O) crossing the charge-ordering transition and the local distortion remains over the whole temperature range. Moreover, the local structure around the Mn atom in these charge-ordered compounds is also not consistent with a linear combination of Jahn–Teller-distorted (Mn^{3+}) and non-distorted (Mn^{4+}) octahedra over the whole temperature range. On the other hand, the structural analysis up to the second coordination shell indicates that the Mn–O–Mn bond angle is the most relevant parameter for understanding the electrical and magnetic properties of these compounds. Finally, an alternative structural mechanism is proposed to explain the different phase transitions in mixed-valence manganites.

1. Introduction

Mixed-valence manganites $(RE_{1-x}A_x)MnO_3$ (RE = rare-earth cation, A = alkali or alkaline-earth cation) with a perovskite structure exhibit a rich variety of crystallographic,

[3] Author to whom any correspondence should be addressed.

electronic and magnetic properties, such as giant magnetoresistance (GMR) near the Curie temperature (T_C) [1]. Extensive study of GMR in $(RE_{1-x}A_x)MnO_3$ oxides has also revealed novel features, including the appearance of so-called charge-ordered (CO) states.

The charge-ordering mechanism has been proposed to explain the insulating and antiferromagnetic behaviour (AFI state) found at low temperatures in the $x \geqslant 0.5$ doping range [2]. Then, samples with $x > 0.5$ exhibit phase transitions with decreasing temperature, accompanied by increase of their electrical resistivity; this is opposite to the cases for $x \approx 0.33$ samples, where a ferromagnetic–metallic state is found in the low-temperature phase.

Changes in the electrical resistivity seem to be associated with structural changes which have been the subject of a wide range of studies. The stability of the CO state relative to that of the ferromagnetic–metallic state depends on the lattice form (tolerance factor of the crystal) and the nominal hole concentration x [3]. Such a charge-ordering state is most likely when the carrier concentration is a rational fraction of lattice points, in particular $x = \frac{1}{8}, \frac{1}{2}$ or $\frac{3}{4}$. The extra fourth d electrons may then be localized on alternate manganese sites below a certain temperature T_{CO} that, for instance, for $La_{0.5}Ca_{0.5}MnO_3$ compound, occurs at values below T_C or even high enough to suppress T_C, as occurs for Tb samples with $x \geqslant 0.5$. This effect is accentuated by small displacements of the oxygen atoms to accommodate the ordered cation lattice, involving, in general, a change in the symmetry of the lattice. The occurrence of the low-temperature antiferromagnetic–insulator state (CO state) also depends on the relative average radii of the rare-earth and alkaline-earth cations [4–6]. Therefore, a charge-ordering behaviour different from that shown by light rare earths (La, Pr, Nd) is expected for heavy rare earths (Sm, Tb) is expected, as the latter induce larger lattice distortions.

On the basis of electron microscopy [7] and x-ray and neutron diffraction experiments [8–14], different charge-ordering models have been proposed to explain the AFI low-temperature phase of these compounds. X-ray resonant scattering experiments at the Mn K edge [15–17] also claim the observation of a 'real' charge and orbital ordering in these manganites. However, the occurrence of charge localization is still a matter of controversy. Recent spectroscopic studies have also cast doubts on a simple model of atomic charge localization [18, 19].

The determination of the local structure is a main goal in attempts to understand the electrical behaviour of these materials, in particular the relationship between the local vibrational modes and the carrier's motion. A great number of works have attempted to determine the local structure around the Mn atom using extended x-ray absorption fine-structure (EXAFS) spectroscopy [20–24] and neutron diffraction [25–27]. Tyson *et al* [20] reached the conclusion that local Jahn–Teller distortions of the paramagnetic phase ($T > T_C \approx 270$ K) of the $La_{0.67}Ca_{0.33}MnO_3$ compound disappeared at low temperatures. Similar conclusions were reached by Billinge *et al* [25] and Hibble *et al* [26] from pair-distribution-function analysis of neutron diffraction data on the $La_{1-x}Ca_xMnO_3$ series. Our previous work on several magnetoresistive $La_{1-x}Ca_xMnO_3$ ($x \approx 0.33$) samples with different T_C-values is in agreement with the different studies [21]. It shows that the Mn atom is surrounded by a regular oxygen octahedron in the metallic–ferromagnetic phase with a value of σ^2_{Mn-O} similar to that obtained for $CaMnO_3$ where there is no Jahn–Teller distortion of the Mn–O bonds. However, it has been suggested by Louca *et al* [27], on the basis of a neutron diffraction study in $La_{1-x}Sr_xMnO_3$ series, that Jahn–Teller distortions remain in the metallic phase ($T < T_C \approx 300$–375 K), although much reduced, even at low temperatures. A similar conclusion was reached by Meneguini *et al* [22], Booth *et al* [23] and Lanzara *et al* [24] in their respective EXAFS studies of $La_{1-x}Ca_xMnO_3$ ($0.2 \leqslant x \leqslant 0.4$) compounds. It is noteworthy that although all of these works propose a distorted configuration, they all give different microscopic descriptions. Clearly, there is controversy in the interpretation of the experimental data as regards the local structure in these doped manganites. Moreover,

a thorough comparison between different series of compounds with different magnetic and electrical behaviours, such as the La–Ca and Tb–Ca series, is still not well established.

In the present paper, we focus attention on the changes in the Mn–O bond length distribution across different charge-ordering transitions. The variation of the local structure at the Mn site, as a function of the doping rate (mainly for $x \geqslant 0.5$ samples) and temperature (20–600 K), is presented for the $La_{1-x}Ca_xMnO_3$ and $Tb_{1-x}Ca_xMnO_3$ series, with the aim of comparing systems with different bandwidths. A comparison of the local structure at the Mn site between ferromagnetic–metallic and charge-ordering compounds is also reported for the La–Ca series in the temperature range from $T = 300$ K up to $2T_C \approx 500$–600 K. In this case, the lattice effects associated with the charge-localized (CL) state, proposed to appear in $La_{2/3}Ca_{1/3}MnO_3$ above $T_C \approx 270$ K [28, 29], are correlated with the effects found in the CO compounds. On the other hand, it has been suggested that the Mn–O–Mn bond angle may play a significant role in the description of the transport properties of these materials, since it determines the matrix element for hopping between Mn sites [4]. Previous spectroscopic studies did not address any changes in the Mn–O–Mn bond angle. Therefore, a multiple-scattering second-shell analysis has also been carried out in order to determine the Mn–O–Mn bond angle distribution and its evolution across the different phase transitions. Finally, an structural model alternative to the pure ionic Mn^{3+} (Jahn–Teller)–Mn^{4+} model is proposed for the different phase transitions and the detailed nature of the structural changes which govern the electronic properties of mixed-valence manganites is discussed.

2. Experimental details

X-ray absorption measurements at the Mn K edge were made on polycrystalline black powder samples, synthesized by conventional solid-state chemistry procedures. The synthesis route and the structural, electrical and magnetic characterizations have been reported elsewhere [11, 14]. All the samples studied were characterized by x-ray powder diffraction, resulting in oxygen-stoichiometric orthorhombic perovskite single phase at room temperature. The dc and ac magnetization were measured using a commercial quantum design magnetometer (SQUID) between 5 and 300 K. La samples with $x = 0$ and 1 show antiferromagnetic (AF) transitions at ∼140 and 120 K, respectively [30]. The $x = 0.33$ sample (GMR) develops a ferromagnetic transition [29] at $T_C \approx 270$ K. The $x = 0.5$ compound [10], upon cooling, first becomes ferromagnetic (∼225 K) and then AF (∼155 K), whereas the $x = 0.67$ sample [11] shows a CO transition at 275 K and an AF transition at 160 K. The magnetic properties of Tb samples, however, are much more complex [14]. $TbMnO_3$ develops a long-range AF ordering at very low temperatures (∼45 K). As the Ca content increases up to $x = 0.33$, a spin-glass-like phase is found at around 50 K. For higher values, $0.45 \leqslant x \leqslant 0.65$, the CO state is stabilized at ∼300 K and then an AF ground state appears below ∼140 K. Table 1 summarizes lattice parameters at $T = 300$ K and magnetic transition temperatures for the whole set of samples.

X-ray absorption experiments were performed in transmission mode on the beamlines BM29 and ID26 at the ESRF. A Si(111) double-crystal monochromator was used. The incident and the transmitted beam were detected by means of ionization chambers with N_2 filling at BM29 and the energy resolution $\delta E/E$ was estimated to be about 1×10^{-4}. Harmonic rejection was achieved by detuning (50%) of the two crystals with respect to the parallel alignment. Spectra were recorded from 20 up to 300 K by means of a closed-cycle helium cryostat with an accuracy of ±1 K. The high-temperature measurements ($T > 300$ K) were carried out at ID26 by means of a controlled-temperature furnace. Silicon photo-diodes were used to record the incident and transmitted flux, providing a full linear energy response. The energy resolution was estimated to be around 1.4×10^{-4}.

Table 1. Crystal structure at room temperature, stoichiometry and magnetic properties (Curie temperature—T_C, charge-ordering temperature—T_{CO} and Néel temperature—T_N) of the $La_{1-x}Ca_xMnO_3$ and $Tb_{1-x}Ca_xMnO_3$ series.

Sample	Mn^{4+} (%)	Space group	Lattice parameters (Å)			T_C (K)	T_{CO} (K)	T_N (K)	Reference
			a	*b*	*c*				
$LaMnO_3$	0	*Pbnm*	5.535	5.723	7.697	—	—	140	[30]
$La_{0.67}Ca_{0.33}MnO_3$	32	*Pbnm*	5.472	5.457	7.711	270	—	—	[29]
$La_{0.5}Ca_{0.5}MnO_3$	50	*Pbnm*[a]	5.435	5.425	7.647	225	155	155	[10]
$La_{0.33}Ca_{0.67}MnO_3$	62	*Pbnm*	5.404	5.379	7.580	—	275	160	[11]
$TbMnO_3$	3	*Pbnm*	5.302	5.856	7.401	—	—	45	[14]
$Tb_{0.67}Ca_{0.33}MnO_3$	34	*Pbnm*	5.326	5.529	7.496	—	—	50	[31]
$Tb_{0.5}Ca_{0.5}MnO_3$	49	*Pbnm*[a]	5.337	5.462	7.472	—	300	140	[8]
$Tb_{0.33}Ca_{0.67}MnO_3$	66	*Pbnm*[a]	5.305	5.353	7.481	—	260	138	[14]
$CaMnO_3$	96	*Pbnm*	5.269	5.281	7.458	—	—	120	[14]

[a] These space groups are taken as rough approximations at low temperatures. A common superstructure has been reported for these compounds below T_{CO}, resulting in a monoclinic cell with a space group $P2_1/m$.

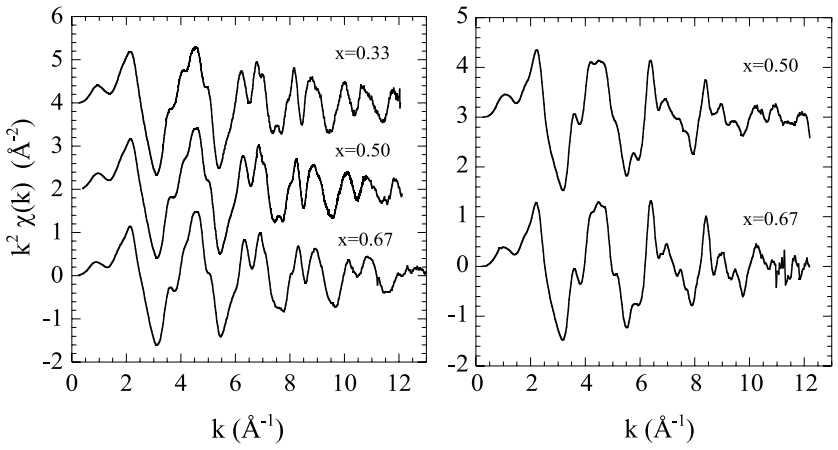

Figure 1. Experimental $k^2\chi(k)$ signals versus k for $La_{1-x}Ca_xMnO_3$ ($x = 0.33$, 0.5 and 0.67) (left panel) and $Tb_{1-x}Ca_xMnO_3$ (0.5 and 0.67) (right panel) samples at room temperature.

Pellets were prepared with boron nitride in order to optimize the thickness of the samples to obtain the best signal-to-noise ratio. The room temperature spectra are identical to those previously reported [21, 32]. Figure 1 shows $k^2\chi(k)$ as a function of the photoelectron wavevector $k \sim \sqrt{(E - E_0)}$ (where E_0 is the experimental threshold energy) for all the samples studied at $T = 300$ K, as an example of data quality. A statistical noise level of the order of 10^{-3} to 10^{-4} characterizes the measurements.

The structural analysis up to $k \sim 12$ Å^{-1} including multiple-scattering terms was performed using the GNXAS package [33]. The goodness of theoretical phases and amplitudes have been checked for the theoretical phases and amplitudes by fitting of the parent compounds, $LaMnO_3$ and $CaMnO_3$. Data analysis is performed by refining a model function in the experimental absorption coefficient using a non-linear fitting procedure in the space of the structural and background parameters (atomic normalization, absorption from other excitations and possible contribution of multielectron channels) [34].

Due to the short mean free path of the photoelectron (∼5–10 Å), the theoretical model $\chi(k)$ signal was calculated as a sum of four single-scattering (Mn–O (first coordination shell), Mn–RE/Ca, Mn–Mn, Mn–O (second coordination shell)) and two multiple-scattering (Mn–O–Mn, O–Mn–O) signals, associated with the local configuration including the photoabsorber (in our case Mn) up to about 4 Å. The different theoretical signals have been calculated on the basis of the orthorhombic *Pbnm* structure of each sample at room temperature (see table 1), using the muffin-tin approximation with an overlap of about 10% between nearest atomic spheres and a Hedin–Lundqvist complex exchange–correlation potential [33]. In this analysis, nine structural parameters were used: interatomic distances and variances $R_{\mathrm{Mn-O}}$, $R_{\mathrm{Mn-RE}}$ (in Tb samples, two different values (6 and 2) were considered), $R_{\mathrm{Mn-O_2}}$, $\sigma^2_{\mathrm{Mn-O}}$, $\sigma^2_{\mathrm{Mn-RE}}$, $\sigma^2_{\mathrm{Mn-O_2}}$; the ⟨Mn–O–Mn⟩ angle; and the ⟨Mn–O–Mn⟩ and ⟨O–Mn–O⟩ angular deviations. High-frequency contributions (single-scattering terms) up to 7 Å have also been included with fixed interatomic distances and variances, according to the crystallographic values. Three other parameters were also taken into account in the fitting process: the energy E_0 was found to be within 4–5 eV with respect to the value determined from the first inflection point of the main edge, a fixed overall reduction factor $S_0^2 = 0.65$ was used for all the fits reported, determined from the $CaMnO_3$ compound, while the energy resolution of the experimental spectra was fixed at the value obtained from the room temperature fitting. Moreover, coordination numbers (N_i) were fixed at the values dictated by the perovskite structure.

The estimated errors reported below are relative errors, based on the relative changes from one temperature to the next, and they do not account for absolute errors. Then, the statistical errors (mainly coming from counting statistics) in the interatomic distances and Debye–Waller factors are estimated by looking at the 95% confidence intervals in the parameter's space, including the correlation with the variables E_0 and S_0^2, respectively [35].

3. Results

Figure 2 shows the modulus of the Fourier transform of $k^2\chi(k)$ for the Mn K-edge data for both the $La_{1-x}Ca_xMnO_3$ and $Tb_{1-x}Ca_xMnO_3$ ($x \geqslant 0.5$) series, at several representative temperatures across the charge-ordering transition.

Well-defined peaks, corresponding to the different near coordination shells around the Mn atom are visible up to about 7 Å. According to the *Pbnm* crystal structure and taking into account the negative phase-shift contribution, the first peak is associated with the oxygen octahedra (MnO_6) while the broad peak centred near 3 Å includes contributions from the Mn–RE/Ca and Mn–Mn pairs as well as from the Mn–O–Mn multiple-scattering configuration. Another peak at about 5.2 Å is mainly due to another shell of 12 Mn atoms and the last peak at about 6.3 Å is related to the presence of both RE/Ca and Mn atoms.

The most relevant feature is that the amplitude of the Mn–O peak is nearly unchanged with decreasing temperature below 300 K in all the samples. Such behaviour, completely opposite to the drastic change reported for the $La_{0.67}Ca_{0.33}MnO_3$ compound across the metal–insulator transition [21], indicates that no dramatic structural changes occur in the local environment around the Mn atom across the charge-ordering transition. Moreover, the undoped compound $CaMnO_3$ exhibits a monotonic behaviour with decreasing temperature in agreement with a Debye model, as will be discussed later on. As the amplitude of the Mn–O peak is directly related to the vibrational amplitude plus a static disorder of the atom-pair distribution, this behaviour suggests that the temperature evolution of the Mn–O bond length distribution is mainly dominated by the presence of static disorder. A similar behaviour was also found for the third peak (around 5.2 Å) of the Fourier transform, related to the Mn–Mn bond length distribution.

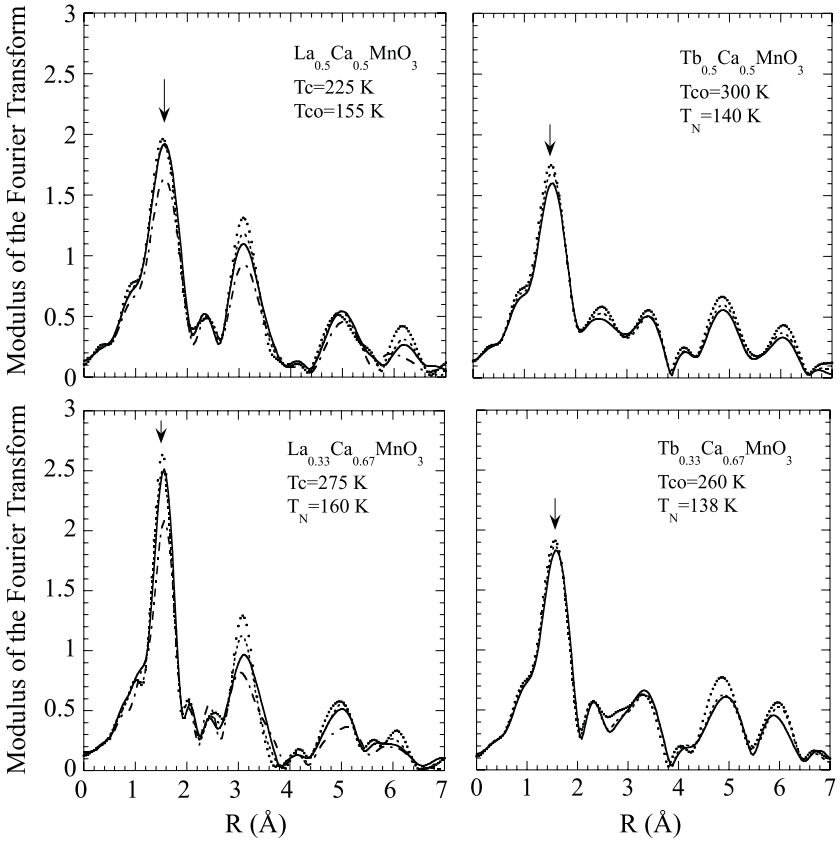

Figure 2. Fourier transforms of the experimental $k^2\chi(k)$ signals for the $La_{1-x}Ca_xMnO_3$ and $Tb_{1-x}Ca_xMnO_3$ samples with $x = 0.5$ and 0.67 at different temperatures across the charge-ordering transitions (— · —: $T > 300$ K; ——: 300 K; - - - -: 200 K; · · · · · ·: 60 K). Data are transformed from 3.5–12 $Å^{-1}$ using a Gaussian window. The Mn–O peak is marked by arrows.

This experimental evidence indicates the presence of substantial changes in the local structure around the Mn atom in Ca-doped manganites with temperature, strongly dependent on the magnetic and electrical properties. In order to extract quantitative information about this local structural effects, we have performed a multiple-scattering EXAFS data analysis using the GNXAS method described in the previous section.

Figure 3 (upper panel) reports the multiple-scattering terms, γ^2 and γ^3, related to the two-atom and three-atom configurations within 4 Å around the Mn site, taken into account for the data analysis in the case of the $La_{0.5}Ca_{0.5}MnO_3$ compound. The resulting structural $\chi_{model}(k)$ signal (dashed curve) and the experimental $\chi(k)$ signal (solid curve) are also reported in the lower panel of figure 3 for all the CO compounds studied at room temperature; they show good agreement. Small discrepancies in the k-range from 7 to 10 $Å^{-1}$ are found, in particular for Tb-doped compounds. These features, not reproduced by the present multiple-scattering calculation, are assigned to higher-frequency contributions due to either distant atoms ($R > 4$ Å) that have been fixed at the crystallographic positions or other three-atom configurations not taken into account in the present analysis. The respective EXAFS spectra have been analysed as a function of temperature in order to quantify the changes in the local structure across the several magnetic and electrical transitions.

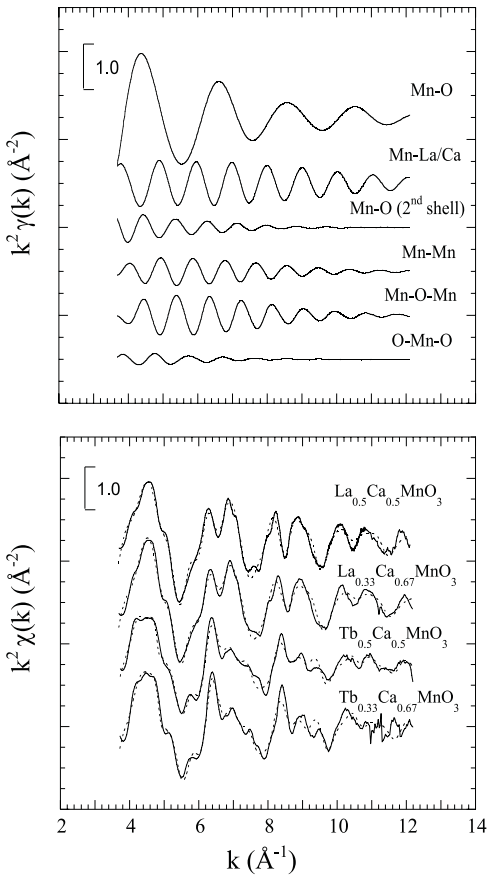

Figure 3. Upper panel: multiple-scattering $k^2\gamma$ signals associated with the main two-atom and three-atom configurations up to 4 Å^{-1} contributing to the total $k^2\chi(k)$ model signal. Lower panel: experimental (solid curve) and best-fit model (dashed curve) $k^2\chi(k)$ signals for $La_{1-x}Ca_xMnO_3$ and $Tb_{1-x}Ca_xMnO_3$ ($x = 0.5$ and 0.67) samples at room temperature.

3.1. First-coordination-shell analysis

Fitting results for the first coordination shell (Mn–O) were obtained directly from the multiple-scattering (MS) analysis, fitting the k^2-weighted raw data over the range $3.7 < k < 12$ Å^{-1}, including all shells up to 4 Å. No isolation of the EXAFS oscillation corresponding to this first Mn–O shell by Fourier filtering was performed. Best-fitting results were obtained considering a single-Gaussian distribution for the six Mn–O distances, as the expected distortion at room temperature is $\leqslant 0.1$ Å [21, 25] and the EXAFS technique does not have enough resolution to separate the contributions at this level.

Best-fitting Mn–O interatomic distances and variances as a function of temperature are summarized in tables 2 and 3 for La-based and Tb-based compounds, respectively. At room temperature, the average Mn–O distance decreases with the formal Mn^{4+} content, $R = 1.892$ Å being the minimum value found for $CaMnO_3$. Very little change of the average Mn–O distance with temperature is shown for all the samples. These results are consistent with diffraction studies within the estimated error. For the $x \approx 0.33$ sample, the average Mn–O distance reported at room temperature is $R_{MnO} = 1.970 \pm 0.005$ Å, approximately constant over the whole temperature range. However, other EXAFS studies show different temperature

Table 2. EXAFS best-fit results for the first oxygen shell of the $La_{1-x}Ca_xMnO_3$ series at the Mn K edge as a function of temperature. N is the coordination number (fixed at 6), R is the interatomic Mn–O distance, σ^2 is the value of the Debye–Waller factor and 'Residual' is the best-fit residual factor. Numbers in parentheses are statistical errors in the last significant digit.

Sample	T (K)	N	R (Å)	σ^2 (10^{-3} Å^2)	Residual ($\times 10^{-5}$)
$La_{0.67}Ca_{0.33}MnO_3$	570	6	1.968(5)	7.8(5)	0.2
	530	6	1.974(5)	7.3(5)	0.3
	500	6	1.971(5)	6.7(5)	0.3
	470	6	1.976(5)	6.7(5)	0.3
	420	6	1.972(5)	6.4(5)	0.3
	370	6	1.971(5)	6.1(5)	0.2
	300	6	1.968(5)	5.2(5)	0.3
	240	6	1.970(5)	3.0(5)	0.8
	90	6	1.969(5)	0.9(5)	1.3
	20	6	1.969(5)	0.6(5)	1.4
$La_{0.5}Ca_{0.5}MnO_3$	470	6	1.960(5)	5.8(2)	0.2
	420	6	1.960(5)	5.4(2)	0.2
	370	6	1.959(5)	4.8(2)	0.2
	300	6	1.956(5)	4.2(2)	0.3
	250	6	1.956(5)	4.1(2)	0.3
	200	6	1.949(5)	4.5(2)	0.3
	175	6	1.944(5)	4.6(2)	0.3
	120	6	1.947(5)	4.5(2)	0.3
	60	6	1.942(5)	4.4(2)	0.4
$La_{0.33}Ca_{0.67}MnO_3$	600	6	1.942(5)	6.4(4)	0.2
	500	6	1.949(5)	5.3(4)	0.2
	430	6	1.939(5)	4.2(4)	0.3
	370	6	1.944(5)	4.0(4)	0.3
	300	6	1.940(5)	3.4(4)	0.5
	250	6	1.939(5)	3.7(4)	0.4
	200	6	1.937(5)	3.7(4)	0.5
	100	6	1.929(5)	3.5(4)	0.5
	60	6	1.931(5)	3.5(4)	0.6

dependences of this average Mn–O bond length for the $x \approx 0.33$ samples. Booth *et al* [23] claim that there is a shrinking of the Mn–O bond around T_C whereas Lanzara *et al* [24] show a slight elongation of this Mn–O bond to occur in the insulating phase. For the CO samples, however, a slightly linear decrease with decreasing the temperature is found. This behaviour has also been addressed by Booth *et al* [23] for the La-based $x = 0.65$ sample.

As the average interatomic Mn–O distance remains nearly constant through these series over the whole temperature range, the main structural effect at the different magnetic transitions is expected to be that on the Debye–Waller factor (σ^2). The temperature evolutions of the Debye–Waller factors for $La_{1-x}Ca_xMnO_3$ ($x = 0.33$, 0.5 and 0.67) and $Tb_{1-x}Ca_xMnO_3$ ($x = 0.5$ and 0.67) samples are shown in figures 4(a) and (b), respectively[4].

If we consider the temperature dependence of σ^2 on the basis of a Debye model plus a temperature-independent contribution related to the presence of static disorder, samples with

[4] Note: bigger values of σ^2_{MnO} than in our previous EXAFS study at RT have been found. Best-fit results were then obtained by least-squares fitting of the Fourier-filtered (between 1 and 2 Å) spectra using the experimental signal of $CaMnO_3$ as reference. The EXAFS signal of $CaMnO_3$ was analysed using theoretical phases and amplitudes generated from FEFF 3.11 code ($\sigma^2_{MnO}(RT) = 0.0015$ Å^2).

Table 3. Best-fit results for the first oxygen shell of the $Tb_{1-x}Ca_xMnO_3$ series at the Mn K edge as a function of temperature. N is the coordination number (fixed at 6), R is the interatomic Mn–O distance, σ^2 is the value of the Debye–Waller factor and 'Residual' is the best-fit residual factor. Numbers in parentheses are statistical errors in the last significant digit.

Sample	T (K)	N	R (Å)	σ^2 (10^{-3} Å^2)	Residual ($\times 10^{-5}$)
$Tb_{0.5}Ca_{0.5}MnO_3$	325	6	1.939(5)	5.7(5)	0.4
	310	6	1.943(5)	5.8(5)	0.4
	290	6	1.941(5)	5.7(5)	0.4
	280	6	1.939(5)	5.7(5)	0.4
	200	6	1.934(5)	5.4(5)	0.5
	100	6	1.927(4)	4.9(8)	0.6
	60	6	1.926(4)	4.9(8)	0.6
$Tb_{0.33}Ca_{0.67}MnO_3$	300	6	1.944(5)	4.8(8)	0.6
	200	6	1.941(5)	4.7(8)	0.7
	60	6	1.932(5)	4.4(8)	0.8

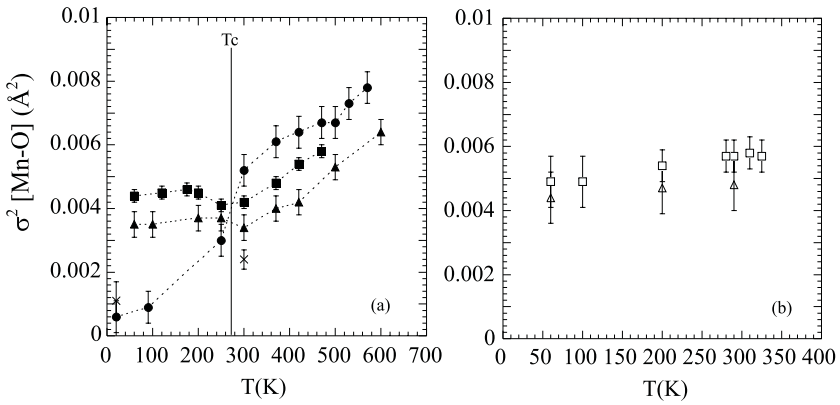

Figure 4. σ^2 versus T for the Mn–O first coordination distance of the (a) $La_{1-x}Ca_xMnO_3$ (●: $x = 0.33$; ■: $x = 0.5$; ▲: $x = 0.67$) and (b) $Tb_{1-x}Ca_xMnO_3$ (□: $x = 0.5$; △: $x = 0.67$) series. Dotted lines are guides to the eye. Data for $CaMnO_3$ (×) are plotted for comparison.

distorted MnO_6 octahedron will show larger Debye–Waller factors. At room temperature, all doped samples show larger Debye–Waller factors, in comparison with the value obtained for the $CaMnO_3$ sample ($\sigma^2 = 0.0024(3)$ Å^2). Moreover, Tb-based compounds show slightly larger Debye–Waller factors than La-based ones (compare tables 2 and 3), according to the more distorted crystallographic structure (the Tb^{3+} ion has a lower ionic radius). This fact suggests a local octahedral environment with a spread of Mn–O distances around the Mn atom at room temperature. Overall, the Debye–Waller factor decreases with the Mn oxidation state. Considering that the distortion of Mn–O distances is of the same type as in the $REMnO_3$ (RE: La, Tb) compounds (Jahn–Teller type), an estimation of the magnitude of this Jahn–Teller distortion (δ = difference between the two long and the four short Mn–O interatomic distances) in the doped compounds from the Debye–Waller factor gives a value of δ ranging from 0.07 Å in the case of the $x = 0.33$ sample down to 0.06 Å in the case of the $x = 0.67$ sample. However, this local distortion is much lower than that reported for pure Jahn–Teller compounds—for example, $\delta = 0.2$ Å for $LaMnO_3$ [21].

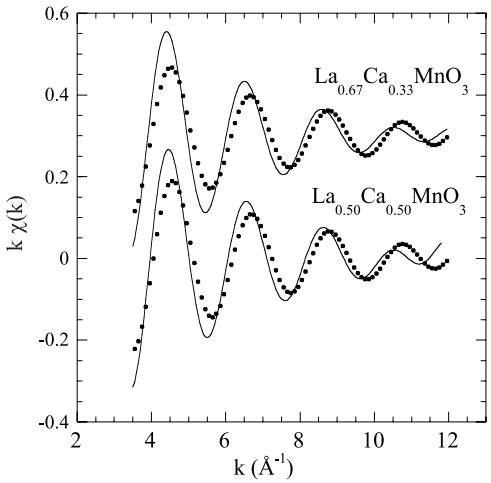

Figure 5. Fourier-filtered $k\chi(k)$ spectra of the first coordination shell (Mn–O) for $La_{0.67}Ca_{0.33}MnO_3$ and $La_{0.5}Ca_{0.5}MnO_3$ samples at room temperature. Experimental spectra (solid curve) and spectra calculated by weighted addition of the end-member ($LaMnO_3$ and $CaMnO_3$) compounds (dots) are compared.

Samples with $x = 0.5$ and $x = 0.67$ show a Debye–Waller factor that is almost independent of the temperature value below the charge-ordering transition for both series of compounds. For the $x \approx 0.33$ sample, however, a drastic change with the temperature is observed on crossing the metal–insulator transition. This anomalous thermal evolution has also been observed by several other authors [22, 23], who claim a polaronic description of the paramagnetic (high-temperature) phase of these compounds giving rise to a distribution of Mn–O distances. Our results show that these octahedral distortions disappear completely at low temperatures, below T_C, when the ferromagnetic metallic state is reached, as the value of the Debye–Waller factor is lower than the one corresponding to the $CaMnO_3$ sample at low temperatures ($\sigma^2 = 0.0011(6)$ Å^2). Therefore, a *static* distortion of the MnO_6 octahedra is proposed to explain the insulating state in the CO samples whereas a *dynamic* distortion, which collapses below T_C, could explain the metal–insulator transition in the $x \approx 0.33$ samples.

In order to determine whether the measured distortions at room temperature (paramagnetic phase) are consistent with a Jahn–Teller polaron model of individual Mn^{3+} and Mn^{4+} sites, we compare the experimental EXAFS signal corresponding to the first Mn–O coordination shell (k-weighted filtered spectra between 1 and 2 Å) for both GMR ($x \approx 0.33$) and CO ($x \geqslant 0.33$) samples, with a weighted addition of the end-member La(Tb)MnO_3 and $CaMnO_3$ signals. Figure 5 shows the results obtained for La-based samples. Clearly, in both cases, the amplitude of the experimental signal at lower k-values is bigger than the calculated one. Moreover, there is also a mismatch in the frequency values of the oscillations. Therefore, the Mn–O local environment in the paramagnetic phase ($T \geqslant 300$ K) cannot be described in terms of the formation of small Jahn–Teller Mn^{3+} polarons.

Finally, there are several works claiming a strong spin–lattice coupling in these materials. In particular, a large magnetovolume effect has been found within the temperature range $T_C < T < T_p$ ($\approx 2T_C$) [28]. In order to check the relevance of the octahedral distortion for this anomalous contribution in the thermal linear expansion, i.e., for the charge localization above T_C, we have also studied the temperature dependence of the structural parameters up to $2T_C$ in the $La_{1-x}Ca_xMnO_3$ series. Our results in figure 4(a) show that no anomalous behaviour is

Table 4. Best-fit results from the structural analysis of the second coordination shell of the $La_{1-x}Ca_xMnO_3$ series at the Mn K edge as a function of temperature. N is the coordination number, R_{Mn-A} and R_{Mn-Mn} are the average interatomic distances for the Mn–La/Ca and Mn–Mn scattering paths and σ^2 is the value of the respective Debye–Waller factor. Numbers in parentheses are statistical errors in the last significant digit.

Sample	T (K)	N	R_{Mn-A} (Å)	σ^2 (10^{-3} Å^2)	N	R_{Mn-Mn} (Å)	σ^2 (10^{-3} Å^2)
$La_{0.67}Ca_{0.33}MnO_3$	570	8	3.381(3)	9.5(3)	6	3.849(15)	15.8(12)
	530	8	3.382(3)	10.3(3)	6	3.840(15)	15.7(12)
	500	8	3.382(3)	10.1(3)	6	3.820(16)	14.7(13)
	470	8	3.384(3)	9.7(3)	6	3.839(15)	14.6(12)
	420	8	3.381(3)	8.8(3)	6	3.842(15)	13.9(12)
	370	8	3.384(3)	8.3(3)	6	3.852(15)	13.2(12)
	300	8	3.385(3)	7.5(3)	6	3.850(15)	11.5(12)
	240	8	3.386(3)	6.5(3)	6	3.855(15)	7.3(11)
	90	8	3.391(3)	5.4(3)	6	3.860(15)	3.2(11)
	20	8	3.389(3)	5.3(3)	6	3.857(15)	2.6(11)
$La_{0.5}Ca_{0.5}MnO_3$	470	8	3.358(5)	9.7(3)	6	3.853(14)	12.4(5)
	420	8	3.362(5)	9.0(3)	6	3.853(14)	11.6(5)
	370	8	3.358(5)	8.7(3)	6	3.848(14)	10.5(5)
	300	8	3.360(5)	8.2(3)	6	3.840(14)	9.5(5)
	250	8	3.359(5)	7.7(3)	6	3.835(14)	9.2(6)
	200	8	3.358(5)	7.4(3)	6	3.812(14)	10.1(6)
	175	8	3.358(5)	7.4(3)	6	3.793(14)	10.4(6)
	120	8	3.362(5)	6.9(3)	6	3.798(14)	10.2(6)
	60	8	3.357(5)	7.0(3)	6	3.788(14)	10.0(6)
$La_{0.33}Ca_{0.67}MnO_3$	600	8	3.335(6)	12.3(4)	6	3.826(14)	13.3(9)
	500	8	3.345(6)	10.7(4)	6	3.839(14)	10.6(9)
	430	8	3.335(6)	10.6(4)	6	3.813(14)	9.3(9)
	370	8	3.346(6)	10.2(4)	6	3.828(14)	9.2(9)
	300	8	3.339(6)	9.7(4)	6	3.816(15)	7.7(9)
	250	8	3.341(6)	9.5(4)	6	3.812(15)	8.5(9)
	200	8	3.341(6)	9.0(4)	6	3.806(15)	8.5(9)
	100	8	3.333(6)	8.4(4)	6	3.786(15)	8.0(9)
	60	8	3.336(6)	8.2(4)	6	3.791(15)	8.0(9)

found for the Debye–Waller factors of the Mn–O distance in the high-T region. Therefore, the charge localization, associated with the paramagnetic phase of these compounds, is not directly related to the Jahn–Teller distortion of the MnO_6 octahedra—opposite to the small-polaron models used to describe the temperature dependence of the resistivity in this region [36].

3.2. Second-coordination-shell analysis

In tables 4 and 5, we report the structural parameters associated with the second coordination shell (Mn–La/Ca and Mn–Mn interatomic distances with the corresponding Debye–Waller factors) for the $La_{1-x}Ca_xMnO_3$ and $Tb_{1-x}Ca_xMnO_3$ series, respectively. The bond distances and variances R_{Mn-Mn} and σ^2_{Mn-Mn} have been evaluated as a function of the floating parameters defining the Mn–O distance and Mn–O–Mn angle distributions as explained in [33].

We found no evidence of any significant change in the temperature dependence of the Mn–La/Ca bond length distribution for all the samples. The best-fitting σ^2-values are in good agreement with a standard Debye thermal evolution, increasing continuously with increasing

Table 5. Best-fit results from the structural analysis of the second coordination shell of the $Tb_{1-x}Ca_xMnO_3$ series at the Mn K edge as a function of temperature. N is the coordination number, R_{Mn-A} and R_{Mn-Mn} are the average interatomic distances for the Mn–Tb/Ca and Mn–Mn scattering paths and σ^2 is the value of the respective Debye–Waller factor. Numbers in parentheses are statistical errors in the last significant digit.

Sample	T (K)	N	R_{Mn-A} (Å)	σ^2 (10^{-3} Å^2)	N	R_{Mn-Mn} (Å)	σ^2 (10^{-3} Å^2)
$Tb_{0.5}Ca_{0.5}MnO_3$	325	6	3.24(1)	12(1)	6	3.750(18)	10.7(13)
		2	3.63(2)	2(2)			
	310	6	3.24(1)	12(1)	6	3.759(18)	10.9(13)
		2	3.63(2)	2(2)			
	290	6	3.24(1)	12(1)	6	3.753(18)	10.7(13)
		2	3.63(2)	2(2)			
	280	6	3.24(1)	12(1)	6	3.750(18)	10.7(13)
		2	3.63(2)	2(2)			
	200	6	3.23(1)	12(1)	6	3.740(18)	10.2(13)
		2	3.63(2)	2(2)			
	100	6	3.23(2)	11(2)	6	3.729(16)	9.2(19)
		2	3.62(2)	1(2)			
	60	6	3.23(2)	11(2)	6	3.724(16)	9.2(19)
		2	3.62(2)	1(2)			
$Tb_{0.33}Ca_{0.67}MnO_3$	300	6	3.26(1)	13(2)	6	3.784(17)	9.2(18)
		2	3.62(2)	2(2)			
	200	6	3.26(1)	13(2)	6	3.778(17)	9.0(18)
		2	3.61(2)	3(2)			
	60	6	3.25(1)	12(2)	6	3.762(17)	8.4(18)
		2	3.59(3)	3(3)			

temperature. Therefore, the reported difference in behaviour with temperature of the second-coordination-shell peak in the Fourier transform between magnetoresistive (see [23] and [26]) and CO samples (see figure 2; the amplitude is almost constant over the whole temperature range) must be related to the Mn–Mn atom-pair distribution.

The $La_{0.67}Ca_{0.33}MnO_3$ sample shows very little change with temperature in the average Mn–Mn bond length (3.850 ± 0.015 Å) across the MI transition (see table 4). However, a shrinking of the distance value is found in the high-temperature region. We will discuss this unexpected result in correlation with the Mn–O–Mn bond angle distribution later on. For the other materials, the Mn–Mn bond length also decreases almost linearly with the temperature across the CO transition (tables 4 and 5).

Figure 6 shows σ^2_{Mn-Mn} versus T. For the $x \approx 0.33$ sample, a temperature dependence very similar to that of the σ^2_{Mn-O}-data (figure 4) is found, including a drastic decrease when T is lowered through T_C.

Results similar to those for the σ^2_{Mn-O}-data (see also figure 2) are also obtained for the CO samples ($x = 0.5$ and 0.67) where the σ^2_{Mn-Mn} are found to be almost independent of the temperature across the charge-ordering transition.

The main factor that controls the difference in magnetic and electrical behaviour between ferromagnetic–metal and AF–CO insulator samples is supposed to be the Mn–O–Mn bond angle. The rare-earth-ion size is directly correlated with the tilting of the MnO_6 octahedra. Consequently, a larger orthorhombic distortion of the unit cell induces a decrease of the average ⟨Mn–O–Mn⟩ bond angle (from 180°), leading to a narrowing in the effective one-electron e_g bandwidth which favours the occurrence of CO phases [14,31]. Therefore, EXAFS

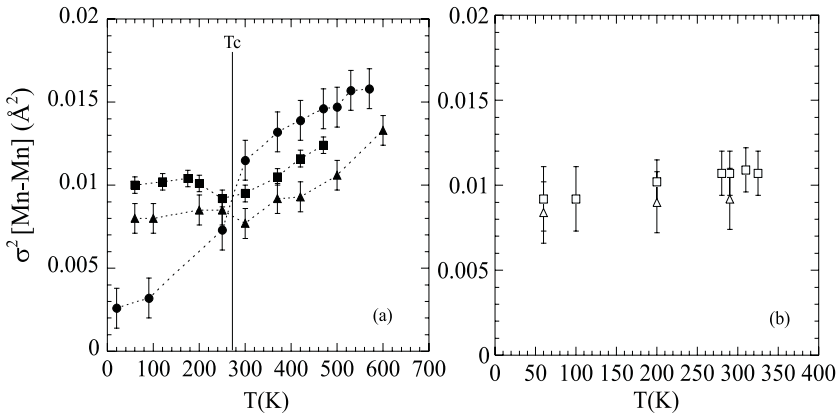

Figure 6. σ^2 versus T for the Mn–Mn interatomic distance of the (a) $La_{1-x}Ca_xMnO_3$ (●: $x = 0.33$; ■: $x = 0.5$; ▲: $x = 0.67$) and (b) $Tb_{1-x}Ca_xMnO_3$ (□: $x = 0.5$; △: $x = 0.67$) series. Dotted lines are guides to the eye.

measurements of the angle distribution across the metal–insulator and CO transitions are particularly interesting for obtaining information about possible changes in the short-range atom distribution due to these phase transitions, complementary to the long-range description obtained by diffraction studies. The thermal evolutions of the ⟨Mn–O–Mn⟩ bond angle value for $La_{1-x}Ca_xMnO_3$ ($x = 0.33$, 0.5 and 0.67) and $Tb_{1-x}Ca_xMnO_3$ ($x = 0.5$ and 0.67) samples are reported in figure 7.

The tilting angle values measured by means of diffraction correspond to a ⟨Mn–O–Mn⟩ bond angle in the range 150°–157° for the intermediate Tb-based compounds [14] and in the range 159°–162° for the intermediate La-based compounds [10, 11, 31]. Our EXAFS data are in agreement with the diffraction values within the experimental error. However, due to the large statistical error in the determination of the angle distributions, we can extract only qualitative information about the different behaviour of these doped compounds as a function of temperature. It has not been possible to detect variations in the ⟨Mn–O–Mn⟩ bond angle distribution with temperature for the Tb samples, as shown in figure 7(b). For the La compounds, CO samples ($x \geqslant 0.5$) show a slight decrease in the ⟨Mn–O–Mn⟩ bond angle with decreasing temperature down to the CO transition temperature. However, no changes are reported for the $x \approx 0.33$ sample across the metal–insulator transition, in the temperature range from RT down to 20 K. We note, however, that an abrupt reduction of this ⟨Mn–O–Mn⟩ angle value clearly occurs at about $2T_C \approx 500$ K. This ⟨Mn–O–Mn⟩ angle contraction might be associated with the presence of strong magnetoelastic effects in the CL paramagnetic–insulator phase of these systems [28,29]. Moreover, further experiments on related compounds are needed in order to obtain relevant information about this effect.

In conclusion, as no change has been reported for σ^2_{Mn-Mn} either in the CO region for $x \geqslant 0.5$ samples or in the CL region for the GMR sample, then the contraction of the Mn–Mn average distance found in these two temperature regions must be due to the reported changes in the ⟨Mn–O–Mn⟩ bond angle configuration.

4. Discussion and conclusions

The local geometrical structure at the Mn site in $La_{1-x}Ca_xMnO_3$ and $Tb_{1-x}Ca_xMnO_3$ samples has been investigated in the range of temperature between 20 and 600 K. The extensive EXAFS study performed on these oxides allow us to get an overall view of the local structure of

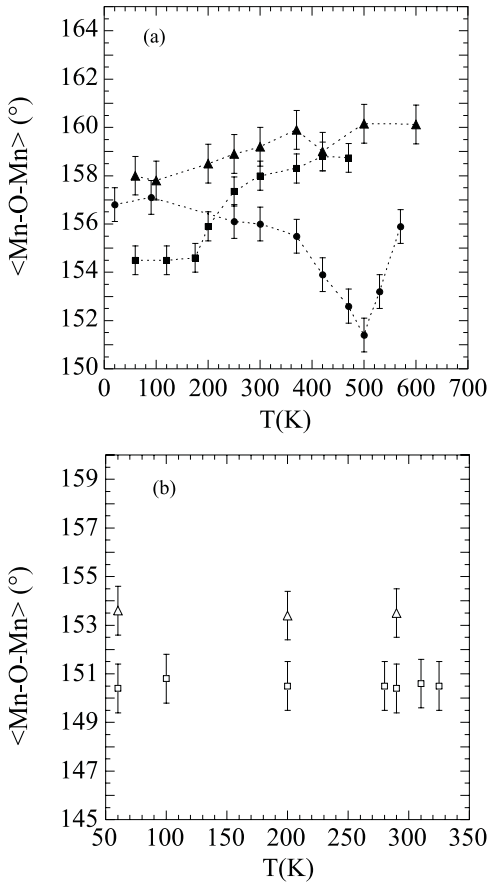

Figure 7. Thermal evolution of the ⟨Mn–O–Mn⟩ bond angle value for the (a) $La_{1-x}Ca_xMnO_3$ (●: $x = 0.33$; ■: $x = 0.5$; ▲: $x = 0.67$) and (b) $Tb_{1-x}Ca_xMnO_3$ (□: $x = 0.5$; △: $x = 0.67$) series. Dotted lines are guides to the eye. Estimated errors for the ⟨Mn–O–Mn⟩ angle are $\pm 1^\circ$.

manganites. The observed changes are qualitatively in agreement with previous studies [23]. However, we can state the following statements, reported earlier, in a clearer form.

(i) The local structure of Mn atoms in the so-called 'charge'-ordered and/or 'orbital'-ordered compounds is practically unchanged at the CO phase transition temperature (see figure 2). In particular, the Debye–Waller factor for the Mn–O distance, for both $x = 0.5$ and 0.67 samples, does not follow the expected behaviour for harmonic thermal vibrations. Either it slightly grows with decreasing temperature or it remains almost constant (see figure 4). Diffraction studies on $x = 0.5$ samples have shown the presence of two different Mn sites at low temperatures, in the CO phase. One site corresponds to a slightly tetragonal distorted MnO_6 octahedron (La sample: $4 \times \langle 1.92\rangle/2 \times \langle 2.06\rangle$ Å; Tb sample: $4 \times \langle 1.90\rangle/2 \times \langle 2.05\rangle$ Å) whereas the other site shows a nearly regular octahedral Mn–O environment ($\langle R\rangle = 1.915$ and 1.945 Å for La and Tb samples, respectively) [8, 10]. Accordingly, the anomalous large Debye–Waller factor observed at low temperatures in our EXAFS analysis for these samples (four times larger than the value corresponding to a regular MnO_6 octahedra; see the data for the $La_{0.67}Ca_{0.33}MnO_3$ sample at low temperatures in table 2 for comparison) can be ascribed to this spread of Mn–O distances.

On the other hand, the high-temperature paramagnetic phase (above the charge-ordering transition) shows only one Mn site with a regular MnO_6 octahedron in the diffraction studies [8–10]. However, the EXAFS results indicate a similar Debye–Waller factor for both high- and low-temperature phases, suggesting that the same local distortions are present in the paramagnetic and CO phases. Bearing in mind that an average distribution is observed using diffraction techniques, one can conclude that the local distortions are dynamic above the charge-ordering transition, i.e. distorted and undistorted MnO_6 octahedra are dynamically changing. This conclusion can be reached by means of the XAS technique, as the interaction time for the x-ray absorption process is much shorter than that corresponding to the atomic motion.

Previous works [23] have interpreted this behaviour in terms of the formation of Jahn–Teller polarons. Distorted and undistorted MnO_6 octahedra were then ascribed to Mn^{3+} (Jahn–Teller) and Mn^{4+} ions, respectively. Therefore, in the paramagnetic phase, the e_g electron of the Mn^{3+} ions (with an electronic configuration: $t_{2g}^3 e_g^1$) jumps into empty e_g orbitals of the Mn^{4+} ions. This process gives rise to a dynamic swap of Mn^{3+}-ion and Mn^{4+}-ion environment in the lattice, resulting in polaronic conduction. However, in the CO phase, the electrons and, therefore, the Mn^{3+} and Mn^{4+} ions are localized in a periodic arrangement in the lattice. This phase transition was then denoted as a charge-ordering transition [1, 37]. This model was supported by several authors [23, 24] but recent experiments have cast doubt on this naive picture. X-ray resonant scattering experiments on several charge-ordering manganites have shown the simultaneous presence of resonances ascribed to charge and orbital orderings [15–17]. Moreover, a discrepancy of 2 eV is observed between the experimental resonance and the expected one from the charge-ordering model. We recently demonstrated that these results could only support a maximal charge disproportionation of ± 0.25 electrons between the two Mn sites [18, 19] and the assumption of the presence of Mn^{3+} and Mn^{4+} ions is not suitable to account for the electronic properties of the so-called charge-ordering compounds. This conclusion is also in agreement with the fact that the two Mn sites in the CO phase show similar magnetic moments as obtained from neutron diffraction patterns [10].

Finally, our EXAFS analysis of the local geometrical structure around the Mn atom does not support the presence of an inhomogeneous mixture of Mn^{3+} and Mn^{4+} ions either. Comparisons of the Mn–O distribution above T_{CO} for various x show that the octahedra distortion of the intermediate compounds is not consistent (see figure 5) with a linear interpolation of the end-member compounds, La(Tb)MnO_3 and $CaMnO_3$, in disagreement with other works [23]. Moreover, the local distortion found in the paramagnetic phase can be considered as 'reminiscent' of the Jahn–Teller one present in the $REMnO_3$ (RE: La, Tb) compounds since it is of the same type for all Mn atoms but the magnitude is severely reduced.

An alternative model is then necessary to account for the experimental results on charge-ordering manganites: we have shown that these compounds have a dynamic local distortion in the paramagnetic high-temperature phase. According with a tetragonal Jahn–Teller distortion, each Mn–O pair presents two lowest potential wells in the free energy, corresponding to short and long Mn–O interatomic distances. The probability of occupying one of the two energy wells is correlated with the occupancy of the rest of the Mn–O pairs in the cluster. At temperatures above the charge-ordering transition, the system has enough energy to jump from one potential well into the other, giving rise to a dynamical structural distortion. However, at low temperatures, there is not enough thermal energy to overcome the energy barrier and each Mn–O pair chooses one potential well, giving rise to an ordered arrangement of the structural distortions. Consequently, the charge-ordering transition could be viewed as an order–disorder transition where the order parameter is mediated by the choice of each Mn–O pair within the lattice. The 'freezing' of these distortions will produce the differentiation of two Mn sites in the crystal structure. Nevertheless, the differences between them must be small, in agreement

with the x-ray resonant scattering, neutron diffraction and EXAFS experiments. In the same way, no significant differences are expected for the Debye–Waller factors at the phase transition, as is shown in figure 4. In fact, this is a simplified model taking into account only the first oxygen coordination shell, but second neighbours may also play an important role in the framework of ordered distortions.

(ii) Second-coordination-shell analysis has indicated that EXAFS spectra are very sensitive to the Mn–Mn distance distribution—in particular, to the Mn–O–Mn three-atom distribution. The average ⟨Mn–O–Mn⟩ bond angle has been found to be slightly dependent on the Ca doping. Differences are found between Tb-based and La-based compounds relating to a larger (or smaller) orthorhombic lattice distortion, which is clearly manifest in a bigger deviation from the ideal 180° for the Tb series. A decrease of the ⟨Mn–O–Mn⟩ bond angle is found to be strongly correlated with the presence of any kind of charge localization (insulating behaviour), either in the low-temperature phase of the so-called CO samples or in the high-temperature region (from 300 K up to $2T_C$) of GMR samples. This temperature behaviour has also been deduced from the crystallographic data on $La_{0.5}Ca_{0.5}MnO_3$ [10] and $La_{0.33}Ca_{0.67}MnO_3$ [13]. The Debye–Waller factor for the Mn–Mn distance behaves as the first-oxygen-shell σ^2_{MnO} does (see figure 6). Moreover, diffraction experiments have also shown an atomic motion for rare-earth atoms at the phase transition temperature [8, 10]. In conclusion, the e_g electron is not confined to a particular atom, as considered for a Jahn–Teller polaron, but is delocalized at the Mn–Mn atomic scale. The electron must be localized in large wavepackets and jumps among different clusters would be the main channel for the electrical conduction. This can also explain other experimental results such as the colossal isotope shift at the CO phase transition in $Nd_{0.5}Sr_{0.5}MnO_3$, which is impossible to address with the traditional Mn^{3+}/Mn^{4+} ordering [38].

Moreover, this model can be enlarged to explain the physical properties of samples without charge-ordering transitions, i.e. $x \approx 0.33$. These samples develop a ferromagnetic phase transition coupled to a metal–insulator transition. The metal ferromagnet is then characterized by a strong decrease of the dynamic distortion of the MnO_6 octahedra [39]. Our EXAFS study confirms this result, as seen in figures 4 and 6. The $x = 0.33$ sample shows a large decrease in the Debye–Waller value, for both Mn–O and Mn–Mn shells, at the ferromagnetic transition. This fact can be interpreted in terms of disappearance of the energy barrier between the two potential wells at T_C. The system, then, shows a single energy well and, accordingly, similar Mn–O distances for all of the Mn–O pairs in the lattice. The appearance of a single well may be driven by long-range ferromagnetic interactions, but it must also be correlated with the doping ratio. An accurate indicator of the changes in the local structure around the Mn atom is the Mn–O–Mn bond angle. Ordered phases show smaller Mn–Mn distances and the ⟨Mn–O–Mn⟩ bond angle becomes smaller than 180°. The sample with $x = 0.33$, however, shows an increase of this bond angle value at T_C (see figure 7), favouring the formation of a single energy well.

Summarizing, our results imply an alternative explanation for the different phase transitions observed in these manganese oxides. All these samples show a dynamical distorted phase at high temperature. With decreasing temperature, the system can stabilize this distortion in two ways. Either the distortion disappears due to the presence of long-range ferromagnetic interactions or the distortion is frozen giving rise to a static ordered (disordered) phase. The competition between these two tendencies could also be responsible for the phase separation phenomenon in manganites [37] that involves two kinds of domain: ferromagnetic metal and ordered insulator. Moreover, various arrangements of the distortions are possible, explaining the large spread of physical properties exhibited by these compounds. The distortions could even be randomly distributed, giving rise to a spin-glass state as reported for the $Tb_{0.67}Ca_{0.33}MnO_3$ compound [31]. However, further detailed studies are needed to fully understand these aspects in the rare-earth–manganese oxides.

Acknowledgments

This work has been supported by the Spanish CICYT project No MAT99-0847. The authors wish to thank the staff of beamlines BM29 and ID26 at the European Synchrotron Radiation Facility (ESRF) for useful discussions and assistance in collecting the data.

References

[1] Coey J M D, Viret M and von Molnár S 1999 *Adv. Phys.* **48** 167–293
[2] Tokura Y, Tomioka Y, Kuwahara H, Asamitsu A, Moritomo Y and Kasai M 1996 *J. Appl. Phys.* **79** 5288–91
[3] Tomioka Y, Asamitsu A, Moritomo Y, Kuwahara H and Tokura Y 1999 *Phys. Rev. Lett.* **74** 5108–11
[4] Hwang H Y, Cheong S-W, Radaelli P G, Marezio M and Batlogg B 1995 *Phys. Rev. Lett.* **75** 914–17
[5] Rao C N R, Mahesh R, Raychaudhuri A K and Mahendiran R 1998 *J. Phys. Chem. Solids* **59** 487–502
[6] Fontcuberta J, Laukhin V and Obradors X 1999 *Phys. Rev.* B **60** 6266–9
[7] Mori S, Chen C H and Cheong S-W 1998 *Nature* **392** 473–6
[8] Blasco J, García J, De Teresa J M, Ibarra M R, Pérez J, Algarabel P A, Marquina C and Ritter C 1997 *J. Phys.: Condens. Matter* **9** 10 321–31
[9] Blasco J, García J, De Teresa J M, Ibarra M R, Pérez J, Algarabel P A, Marquina C and Ritter C 1997 *Phys. Rev.* B **55** 8905–10
[10] Radaelli P G, Cox D E, Marezio M and Cheong S-W 1997 *Phys. Rev.* B **55** 3015–23
[11] Ibarra M R, De Teresa J M, Blasco J, Algarabel P A, Marquina C, García J, Stankiewicz J and Ritter C 1997 *Phys. Rev.* B **56** 8252–6
[12] Fernández-Diaz M T, Martínez J L, Alonso J M and Herrero E 1999 *Phys. Rev.* B **59** 1277–84
[13] Radaelli P G, Cox D E, Capogna L, Cheong S-W and Marezio M 1999 *Phys. Rev.* B **59** 14 440–50
[14] Blasco J, Ritter C, García J, De Teresa J M, Pérez J and Ibarra M R 2000 *Phys. Rev.* B **62** 5609–18
[15] Murakami Y, Kawada H, Tanaka M, Arima T, Moritomo Y and Tokura Y 1998 *Phys. Rev. Lett.* **80** 1932–5
[16] Von Zimmerman M, Hill J P, Gibbs D, Blume M, Casa D, Keimer B, Murakami Y, Tomioka Y and Tokura Y 1999 *Phys. Rev. Lett.* **83** 4872–5
[17] Nakamura K, Arima T, Nakazawa A, Wakabayashi Y and Murakami Y 1999 *Phys. Rev.* B **60** 2425–8
[18] García J, Sánchez M C, Subías G and Blasco J 2001 *J. Phys.: Condens. Matter* **13** 3229–41
[19] García J, Sánchez M C, Blasco J, Subías G and Proietti M G 2001 *J. Phys.: Condens. Matter* **13** 3243–56
[20] Tyson T A, Mustre de León J, Conradson S D, Bishop A R, Neumeier J J, Röder H and Zang J 1996 *Phys. Rev.* B **53** 13 985–8
[21] Subías G, García J, Blasco J and Proietti M G 1998 *Phys. Rev.* B **57** 748–54
Subías G, García J, Blasco J and Proietti M G 1998 *Phys. Rev.* B **58** 9287–93
[22] Meneguini C, Cimino R, Pascarelli S, Mobilio S, Raghu C and Sarma D 1997 *Phys. Rev.* B **56** 3520–3
[23] Booth C H, Bridges F, Kwei G H, Lawrence J M, Cornelius A L and Neumeier J J 1998 *Phys. Rev.* B **57** 10 440–54
[24] Lanzara A, Saini N L, Brunelli M, Natali F, Bianconi A, Radaelli P G and Cheong S-W 1998 *Phys. Rev. Lett.* **81** 878–81
[25] Billinge S J L, DiFrancesco R G, Kwei G H, Neumeier J J and Thompson J D 1996 *Phys. Rev. Lett.* **77** 715–18
[26] Hibble S J, Cooper S P, Hannon A C, Fawcett I D and Greenblatt M 1999 *J. Phys.: Condens. Matter* **11** 9221–38
[27] Louca D, Egami T, Brosha E L, Röder H and Bishop A R 1997 *Phys. Rev.* B **56** R8475–8
[28] Ibarra M R, Algarabel P A, Marquina C, Blasco J and García J 1995 *Phys. Rev. Lett.* **75** 3541–4
[29] De Teresa J M, Ibarra M R, Blasco J, García J, Marquina C, Algarabel P A, Arnold Z, Kamenev K, Ritter C and von Helmolt R 1996 *Phys. Rev.* B **54** 1187–93
[30] Ritter C, Ibarra M R, De Teresa J M, Algarabel P A, Marquina C, Blasco J, García J, Oseroff S and Cheong S W 1997 *Phys. Rev.* B **56** 8902–11
[31] Blasco J, García J, De Teresa J M, Ibarra M R, Algarabel P A and Marquina C 1996 *J. Phys.: Condens. Matter* **8** 7427–42
[32] Subías G, García J, Proietti M G and Blasco J 1997 *Phys. Rev.* B **56** 8183–91
[33] Filipponi A, Di Cicco A and Natoli C R 1995 *Phys. Rev.* B **52** 15 122–34
Filipponi A and Di Cicco A 1995 *Phys. Rev.* B **52** 15 135–49
[34] Filipponi A and Di Cicco A 2000 *Task Q.* **4** 575–669
[35] Filipponi A 1995 *J. Phys.: Condens. Matter* **7** 9343–56
[36] Friedman L and Holstein T 1963 *Ann. Phys., Lpz.* **21** 494
[37] Dagotto E, Hotta T and Moreo A 2001 *Phys. Rep.* **344** 1–153
[38] Zhao G, Ghosh K and Greene R L 1998 *J. Phys.: Condens. Matter* **10** L737–42
[39] Radaelli P G, Marezio M, Hwang H Y, Cheong S-W and Batlogg B 1996 *Phys. Rev.* B **54** 8992–5